The impact of mechanical characteristics of GDL on the efficiency of a PEM fuel cell

Klara Olli

March 2022, Lund

This degree project for the degree of Master of Science in Engineering has been conducted at the Department of Energy Sciences, Faculty of Engineering, Lund University, and at PowerCell Sweden AB, Gothenburg.

Supervisor at Lund University was Professor Bengt Sundén.
Supervisor at PowerCell was Gabor Toth and Marcus Ringström.
Examiner at Lund University was Professor Magnus Genrup.

Thesis for the Degree of Master of Science in Engineering

ISRN LUTMDN/TMHP-22/5490-SE

ISSN 0282-1990

Department of Energy Sciences
Faculty of Engineering, Lund University
Box 118, 221 00 Lund
Sweden

www.energy.lth.se

Abstract

When a fuel cell stack is assembled it is compressed to ensure gas tightness, and as a consequence, the Gas Diffusion Layer (GDL) will intrude into the channels of the Bipolar Plate (BPP). In this work, the GDL is studied in compression tests and through intrusion measurements. Based on the collected data from the measurements, an approximative method is developed to calculate the intruded profile and stack pressure drop.

The approximated function to describe the intrusion was estimated by a cosine curve with input parameters such as BPP geometry and the difference in uncompressed and compressed thickness of the GDL. The function was found to fit well to the measured values, and the calculated values for the stack pressure drop correspond moderately to real measured test values with some error margin. Overall it could be found that a GDL material with a larger intrusion profile will result in an increase in the stack pressure drop, hence decrease the total fuel cell system efficiency.

Contents

1 Introduction

1.1 Project Background

The world is going through an electrifying transformation, and towards this conversion fuel cells look like promising candidates among sustainable options. A fuel cell is an energy converter that turns the chemical energy from the fuel (e.g. hydrogen) into electrical energy and heat. There are several fuel cell technologies available and adapted to industries for examples in the aerospace, automotive industries, and for stationary use. The biggest difference between the various fuel cell technologies is the operating temperature and material used in the electrolyte and electrodes.

A Proton Exchange Membrane (PEM) fuel cell is a type that operates at low temperature ($\sim$ 80 °C) and can be designed relatively small and lightweight [1]. Due to its smaller dimensions, the PEM fuel cell can be manufactured at a relatively low cost. It has also quite high conversion efficiency, emits zero emissions, and the lifetime is predicted to be long since it has no moving parts.

When speaking of a fuel cell it is usually referred to as a stack, a group of stacked unit cells. A single cell consists of the PEM in a sandwich structure with other components that enable and support the electrochemical process of which approximately 1 V can be obtained [2]. The cells are stacked in series to enable higher output. To get the fuel cell stack operational, it needs a supporting system to:

1. Supply reactant gases and transfer the exhaust
2. Regulate the temperature in the stack and remove the heat
3. Regulate the power output
4. Handle the startup, operation, and shutdown

The efficiency of the whole system is dependent on the fuel cell stack, as well as on the required power needed to run the supporting system. There are a lot of parameters that can influence the resulting efficiency, but the present Master thesis work has been narrowed down to just study the fluid flow, more specifically the fluid pressure drop.

A real phenomenon that can influence the pressure drop is the intrusion between the two components Bi-Polar Plate (BPP) and Gas Diffusion Layer (GDL). The BPP directs the reactant gases and the cooling media in the fuel cell with a channel patterned structure build from two metallic sheets. The GDL on the other hand is made up of a porous material to further transfer the reactant gases. To ensure gas tightness the whole stack is compressed, and the GDL will intrude into the BPP channels. The cross-sectional area of the channel will then shrink and the pressure drop increase.

1.2 Objectives

The main objective of this work is to study how the intrusion phenomenon influence the overall efficiency of a fuel cell system. This will initially be done by characterizing the mechanical properties and behavior of different GDL materials. The next step is to collect data from intrusion measurements, where the BPP geometry can be varied in the test setups with the help of a special-designed fixture. The intrusion properties in combination with specific mechanical characteristics will provide the necessary data

to predict the intrusion of GDL in the real channel geometry of the BPP with a simple analytic model. From the analytic model, the pressure drop in the channel can be estimated, and hence an analysis of how the fuel cell system efficiency is affected.

1.2.1 Problem Statements

The overall goal of the master thesis project is to give an answer to the following question; How do the mechanical characteristics of the GDL impact the efficiency of a PEM fuel cell system?

To find the answer to this overall question, the work can be divided into the following subquestions:

- What happens with the GDL when it is subjected to a compressive force?
- How can the intruded profile be approximated?
- How is the stack pressure drop affected by the intrusion?
- How is the system performance related to the fuel cell stack pressure drop?

2 Theory

2.1 The Fuel Cell Working Principle

A fuel cell is in many aspects similar to a battery, but to get it operational it needs fuel constantly provided. The main part of the cell consists of the anode, cathode, and electrolyte. At the anode, fuel in form of hydrogen is supplied and with help from a catalytic material, the protons and electrons in the hydrogen molecule are split up. The protons can move through the electrolyte, while the electrons are forced to go through an electric circuit. Oxygen is fed from the cathode in form of air, and with the protons and electrons re-joined, water is formed through another electrochemical process [1, 2]. Equations 1 and 2 explain how each of the reactions takes place at both the anode and cathode, while Equation 3 shows the overall reaction. The working process of the fuel cell is illustrated in Fig. 1.

$$Anode: \quad H_2 \rightarrow 2H^+ + 2e^- \tag{1}$$

$$Cathode: \quad \frac{1}{2}O_2 + 2H^+ + 2e^- \rightarrow H_2O \tag{2}$$

$$Overall: \quad H_2 + \frac{1}{2}O_2 \rightarrow H_2O \tag{3}$$

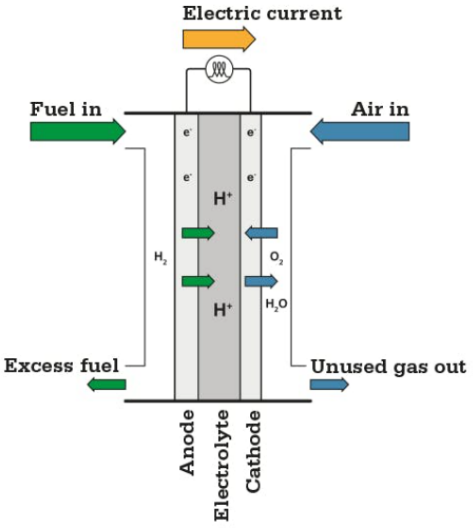

Figure 1: The fuel cell working principle [3].

The overall process is exothermic, which means that energy will be released. With help from Gibbs free energy, it can be shown that 1.23 V can theoretically be earned from the process, which is the maximum voltage that can be obtained from a single cell. This can be translated to an efficiency of 83 %, but the actual output is lower due to losses caused by heat, ohmic resistance, and mass transport.

2.2 The Components in a PEM Fuel Cell

A PEM fuel cell consists of a 7 layers sandwich structure as illustrated in Fig. 2. All merged layers are referred to as the membrane electrode assembly (MEA). The core of the MEA is made of a proton conductive polymer membrane, where Nafion is a common material used and it contains sulfonic acid side chains. The proton transport through the membrane is possible because of the presence of water [1].

The membrane is coated with the next layer, namely the catalyst layer (CL). A common catalyst is platinum, which is mixed together with carbon black into a powder. To transfer the powder to the membrane, it is formed into a slurry and then coated onto the PEM [4]. When a membrane is merged with the CL it is called a Catalyst Coated Membrane (CCM).

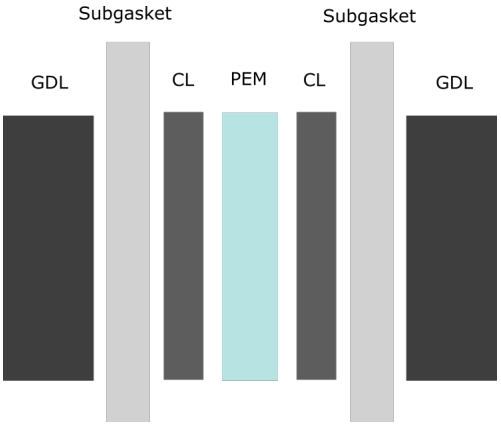

Figure 2: A 7 layer MEA.

When a fuel cell is operating, both heat and water will occur as residual products. But to get a fuel cell in operation, the gases such as fuel and air must be provided to the CL. The Gas Diffusion Layer (GDL) is a porous material that makes the gas flow possible, in the same time it acts as a medium to help transfer the heat and water from the electrochemical processes. The GDL together with the CL makes up the electrode, the part of the cell where the electrons can be transfered.

The last layer of the MEA is the sub gasket, a polymer material that makes sure the whole assembly remains together. The sub gasket encloses the CCM and with a small glued edge it attaches the GDL on each side of the sandwich construction [5]. The shape of the sub gasket is dependent on the BPP since it also works as an insulating layer to prevent a short circuit from the anode and cathode BPP channels.

The critical role of the BPP is to smoothly direct the gases to enable the electrochemical process. From this process, unwanted heat is released, and here the BPP plays a secondary role. The BPP is designed with a channel pattern that makes gas transport possible, but also with channels for the cooling medium to transfer away the generated heat. Fig. 3 illustrates a few layers with MEA and BPP.

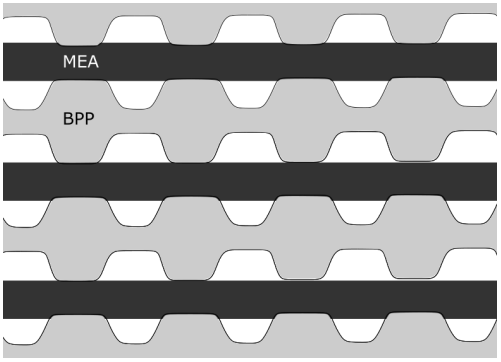

Figure 3: How the MEA and BPP are assembled.

2.2.1 The Gas Diffusion Layer

There are a few demands for the GDL. First, it needs to be a porous material so that the gas and water can transfer through the layer. But it also has to be electrically and thermally conductive to be a medium for the electrons and heat to transfer. The last requirement is that the GDL has to be relatively stiff and flexible. This since it needs to support the rest of the MEA from a mechanical perspective [2].

Carbon fiber is widely used in the industry and fulfills these requirements. The carbon fibers used in the GDL are most commonly produced from PAN-polymer (polyacrylonitrile), mainly because of its low cost and advantageous properties in comparison to other alternatives [6]. The fibers in the GDL are organized in a macro-porous structure, where two different alternatives are used; carbon paper and carbon cloth. The diameter of the fibers is between 5-15 µm [4].

Carbon paper is a non-woven material where the fibers are randomly aligned. The orientation of the fibers can be stretched out so they lay straight which will generate a stiffer material (Fig. 4a) in comparison to a more flexible one where the fibers are organized similar to a spaghetti pattern (Fig. 4b). To keep the fibers together, they are glued with a binder material. Carbon cloth on the other hand is a woven material (Fig. 4c), and in contrast to carbon paper, it does not need a binder material to hold the fibers together [7]. The carbon cloth-based GDL shows better performance under high-humidity conditions for an operating fuel cell, but the opposite is valid for dry conditions where the carbon paper performs superior.

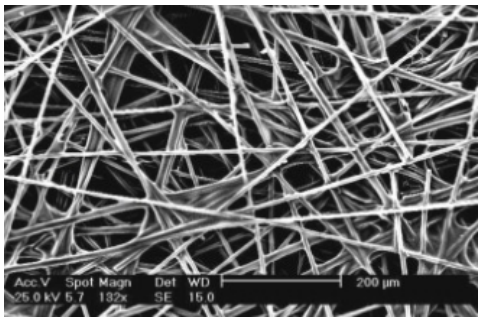

(a) Carbon paper - rigid structure

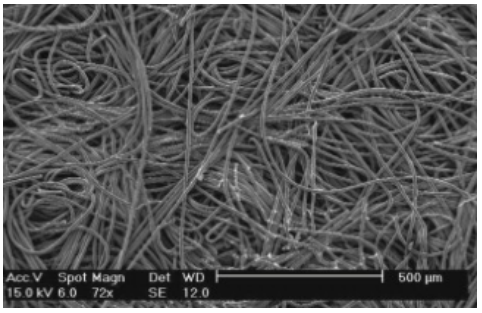

(b) Carbon paper - flexible structure

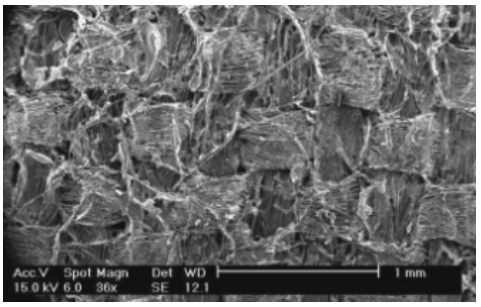

(c) Carbon cloth

Figure 4: Different carbon structures used for the GDL [8].

A step in the manufacturing process of the GDL is to ensure that it receives hydrophobic character to transport liquid water better through the media, which is achieved by treating the material with Polytetrafluoroethylene (PTFE). Water that needs to transfer through the GDL has a tendency to accumulate and block the pores which can evolve into flooding, which will decrease the gas permeability, hence also decreasing the overall performance of the fuel cell. But a too high loading of the PTFE is proved to decrease the electrical conductivity, thermal conductivity, permeability, and porosity of the GDL, which can also result in lower performance of the fuel cell [4, 9].

Another way to gain better water transport quality is to treat the GDL side facing the CL with a mixture of carbon black and PTFE [10]. This coating is called a microporous layer (MPL). The main reason to add the MPL is to decrease the contact resistance between the GDL and CL, but the MPL is proved to also increase the cell performance with more efficient water transport and to mechanically strengthen the GDL[11].

The GDL is a material with anisotropic character, meaning that its properties are dependent on the direction [12]. For example, this includes properties such as mechanical strength, gas permeability, electrical and thermal conductivity. Figure 5 illustrates the directions of a cross-sectional GDL sample. The x-direction is more often referred to as Machine Direction (MD) from the direction of how the GDL roll is stored from the line production. The z-direction is a 90° shift in comparison to MD, therefore it is called the Cross-machine Direction (XD). The Through Plane (TP) direction of the material is defined as the y-direction.

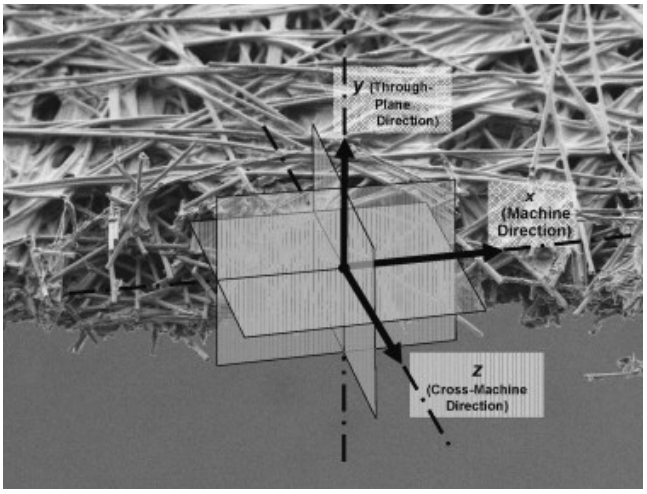

Figure 5: A SEM cross-section view of a GDL including coordinate system with its directions [12].

2.2.2 The Bi-Polar Plate

Similar to the GDL, the BPP needs to be conductive since it is a part of the electrode. But it has also a few other demands like possessing high mechanical strength, being corrosion resistant in order to not poison the PEM, and be designed with a micro-channel pattern for oxygen, hydrogen, and cooling fluid. In a stack, all the BPPs needed make 60-80 % of the total weight, 50 % of the volume, and 35-45 % of the cost [13]. Therefore, the material chosen for the BPP is of great importance. Options used in both industry and research are made from either graphite, composite, or metal.

Graphite has an advantage as it comes to corrosion resistance, but the manufacturing options are limited to use of CNC, which is precise but takes a lot of time, hence not a price efficient method [14]. BPP made out of composites can be manufactured by either injection molding or hot pressing. To increase the electrical conductivity, the composite material has a loading by volume of carbon between 60-90 % [4]. This will result in a brittle material that is difficult to form into thin plates ideal for the fuel cell stack. Due to the high manufacturing cost for the graphite BPP, and the disadvantage of not obtaining a thin design for the composite BPP, they are not as commonly found in the industry as the metallic BPP.

The metallic BPP are typically made out of two thin sheets of stainless steel, which are formed into two Single Polar Plates (SPP) [15]. The shape of the SPP is obtained by a stamping process, but other options like hydro-forming or rolling are also available. The next step in the manufacturing process is to weld the two SPP together. The number of welds can increase the electrical conductivity, but it also increases the manufacturing cost. In order to minimize the contact resistance and to further increase corrosion resistance, the BPP surface is coated with a thin carbon black layer [16].

A limitation with the stamping process for metallic BPP is the design which needs to have a curved cross-sectional profile for the channels. More options are available for the CNC manufactured plates, where the design can take the shape of a rectangular

or a trapezoidal cross-section [14].

2.3 The Intrusion Phenomenon

When a fuel cell is assembled it is compressed to ensure gas tightness. Due to this overall compression, the MEA will be deformed between the two BPPs. Because of the pattern in the BPP, the utmost layer of the MEA, the GDL, will intrude into the BBP channels. This phenomenon is referred to as intrusion.

The ideal stack assembly pressure is between 1.0-2.0 MPa depending on the BPP design [17]. In a compressed state, the contact resistance between the MEA and BPP will decrease, which will lead to an increased stack performance. However, too high assembly pressure will decrease the performance. This is so as the gas permeability will be affected [15, 10].

The porous structure in the GDL will change when the material undergoes compression [18]. The applied force influences the binder material between the fibers by damaging it mechanically, which leads to a re-arrangement of the structure. This re-arrangement is irreversible, meaning that when the GDL has once been compressed it cannot return to its initial state [19]. Depending on the mechanical strength of the fibers in the GDL, they will be almost completely unaffected by the assembly force, but it may happen that some weaker fibers break. If these fibers are pointing out into the channels, they may disturb the fluid flow, or be a potential spot for where water can accumulate [18].

With increased stack assembly force follows a higher intruded profile for the GDL. The more the material intrudes, the more will the cross-sectional area of the channel shrink, which will result in an increase of the fluid flow velocity and the pressure drop over the whole channel [14]. Several other factors can influence the outcome of the intrusion profile. For example, the mechanical properties between MD and XD of the GDL can differ due to the anisotropic behavior of the material, resulting in a lower intrusion profile for the direction with the highest mechanical strength [20].

The BPP design has also a certain impact, where an increase of the channel to rib ratio can result in more intrusion [14]. Due to the small variations within the tolerances from the BPP manufacturing, there might be an uneven force distribution over the GDL.The irregular force distribution may as well occur on the ground of misalignment of the BPP [21]. In an ideal case the anode and cathode channels are perfectly aligned towards each other, but since the channel widths are less than 1 mm a small misalignment can affect the distribution of the applied force, which in turn will impact the intrusion.

To summarize, the following parameters have influence on the intrusion:

1. Material characteristics of the GDL
2. Direction of the GDL (MD or XD)
3. The stack assembly pressure
4. The design of the BPP
5. The alignment of the anode and cathode BPP

2.4 A Fuel Cell System

The supporting system needed to have the fuel cell stack operational, includes subsystems like fuel and air supply, cooling system, water management, electronics for power functioning, and control system [2]. The subsystems influencing the fluid flow, hence the fluid pressure drop, are the fuel and air supplies.

At the cathode inlet, there is a compressor supplying air to the stack. This component consumes significantly much more power than to the rest of the components needed for the air supply [22]. For a case where the pressure drop over the stack is increased, the compressor can compensate with a higher inlet pressure to the stack to not choke the fluid flow. A higher stack inlet pressure means that the compressor needs more power during operation, which in turn decreases the fuel cell system performance since the compressor operates with a share of power from the fuel cell output [23].

For the supply of hydrogen at the anode side, there is a pressure control valve regulating the needed fuel. A common way to ensure that all of the fuel is consumed is to integrate a hydrogen recirculating system that is run by a pump. The power consumption for the valve is negligible in comparison to the pump [22]. Similar to the compressor, the power needed to run the pump increases depending on the pressure drop from the stack.

The reason to compensate for the pressure loss that occurs over the stack is to maintain the Balance of Plant (BOP). This is to ensure the correct water removal to not dry out the membrane or to accumulate water leading to flooding. Both cases lead to a state where the fuel cell operates dysfunctionally.

3 Method

3.1 Sample Information

In the experiments three different GDL materials have been tested; labeled A, B, and C. All are treated with PTFE and coated with an MPL. In Fig. 6, images taken with an optical microscope (Leica DVM6 with objective PLANAPO FOV 3.6) are visible. The images to the left show the untreated side of the GDL, while the right side shows the MPL coated side.

For some of the measurements a CMM sample has been added. The thickness of the CCM is 42 µm.

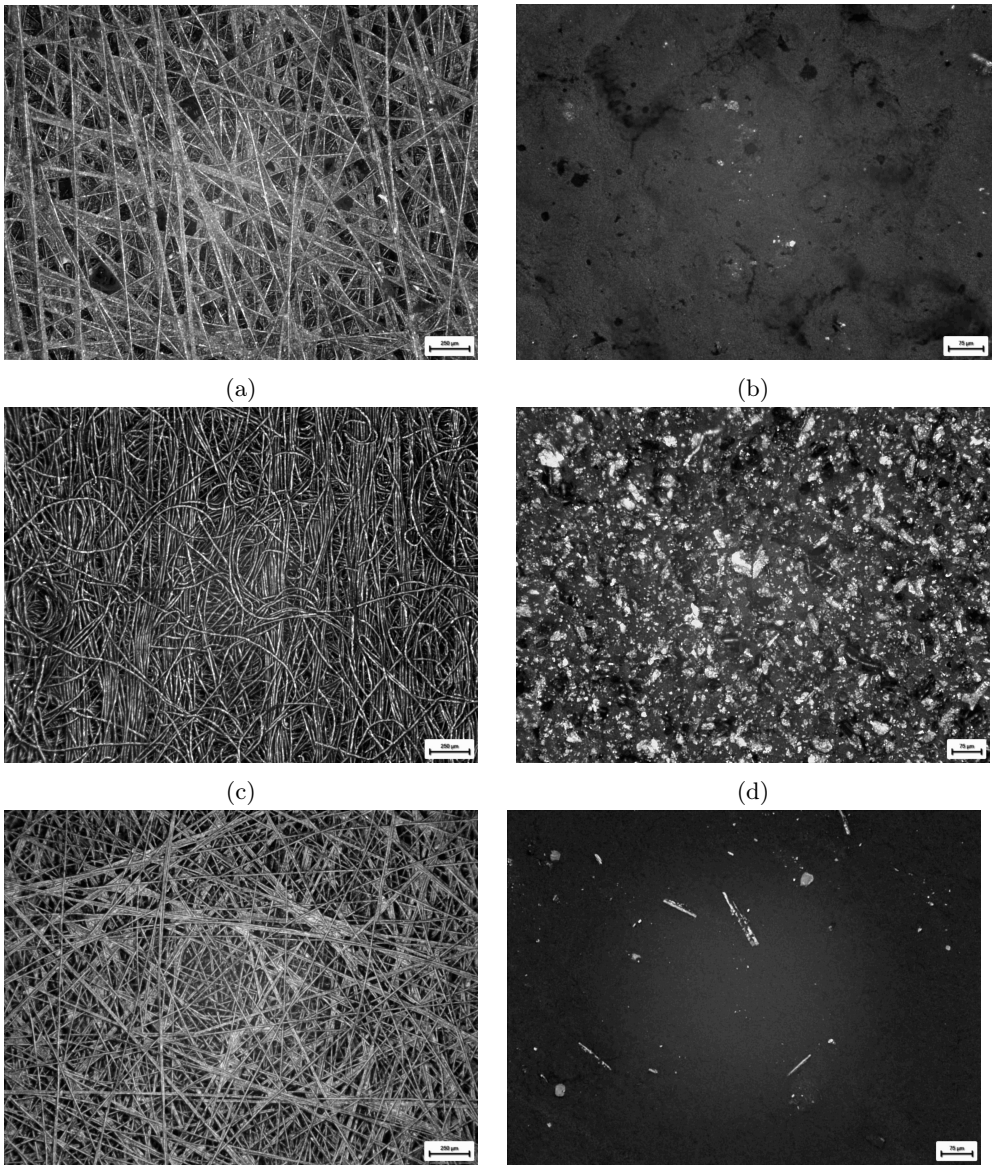

(a) (b)

(c) (d)

(e) (f)

Figure 6: Sample A is represented in images 6a and 6b, sample B in 6c and 6d, and sample C in 6e and 6f.

3.2 Compression Test

The thickness of the GDL depends on how much the material is compressed. Therefore a compression test is performed. A static test machine (hence refereed to as the Zwick) with a compression test fixture is used, which is shown in Fig. 7.

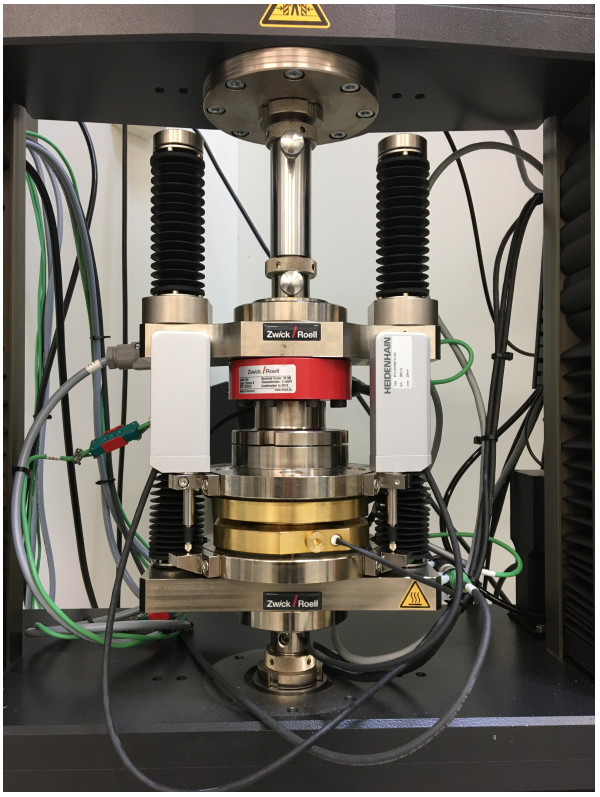

Figure 7: The compression test fixture.

First, a single layer GDL is tested with the dimensions 80x80 mm. The Zwick is programmed to start measuring at the initial pressure of 0.025 MPa, a small pressure that refers to an uncompressed state. The sample is then compressed to a pressure of 2 MPa and this is kept for 60 s. Then, the sample is relaxed back to the initial pressure where the pressure is kept constant once again for 60 s. These steps are repeated in total 4 times according to the cyclic compression visualized in Fig. 8, except for the last 5th cycle where the pressure is kept for 3 min. Five samples of each GDL material are tested.

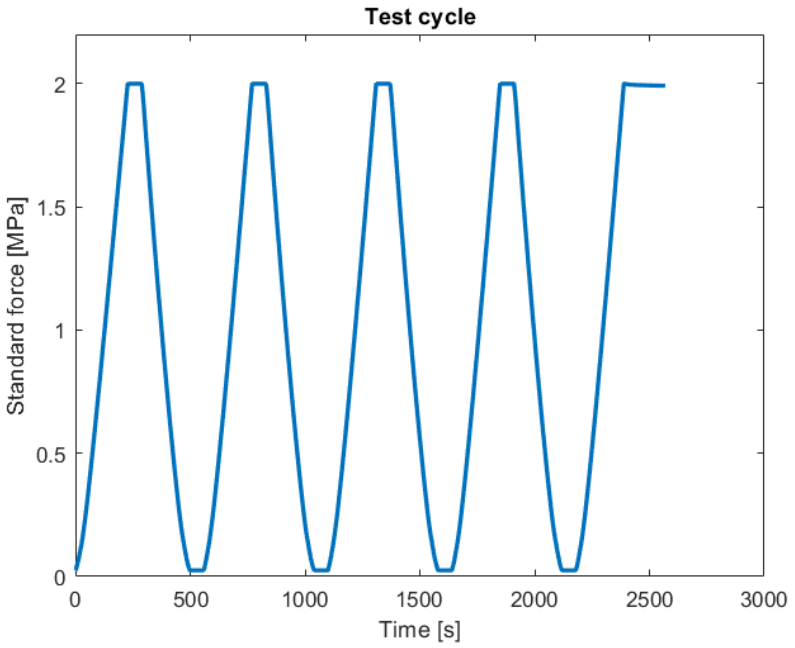

Figure 8: The test cycle used for the compression test

The test procedure is repeated, but instead of only testing one layer of GDL, a small sandwich consisting of two layers of GDL and a CCM sample between them is used. The sample size for the CCM is the same as that used for the GDLs.

3.3 Intrusion measurements

3.3.1 Test Setup

The intrusion phenomenon can be observed by studying the smallest symmetry in a fuel cell, that is the MEA, anode, and cathode channel. In this experiment, the sample will consist of two GDL layers and one piece of CCM, where the sample size for both GDL and CCM is 34x15 mm^2. The small sandwich structure is inserted in a fixture designed for these specific intrusion measurements, which can be observed in Fig. 9.

Figure 9: The Intrusion test fixture.

Various BPP templates with different geometries are tested. One of the templates is shown in Fig. 10. The area of the middle plate where the channel is milled out is 15x15 mm^2. Figure 11 illustrates how the channel geometry is defined and Table 1 summarizes the nomenclature and the units.

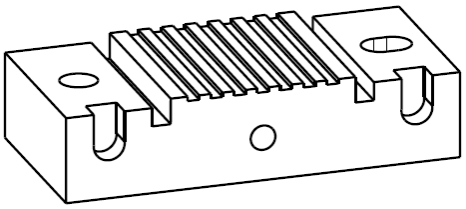

Figure 10: A typical BPP template.

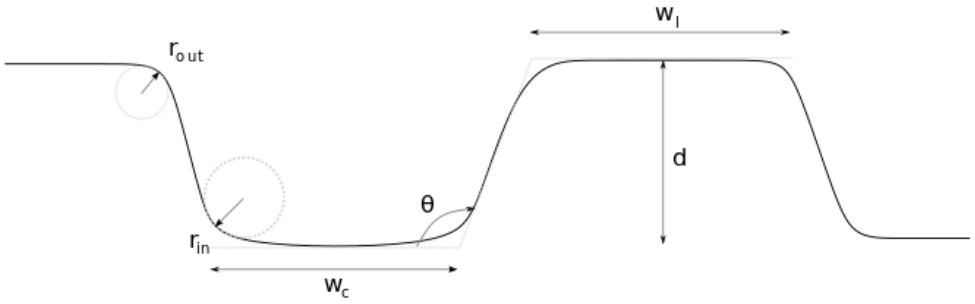

Figure 11: A cross-section of the channel.

	Parameter
d	Channel depth [mm]
w_c	Channel width [mm]
w_l	Land width [mm]
r_{in}	Inner radii [mm]
r_{out}	Outer radii [mm]
θ	Angle from channel bottom to wall [°]

Table 1: A summary of the nomenclature and units for the BPP geometry

The BPP templates will be tested in pairs of anode and cathode. In total 6 different pairs are tested, three with a rectangular cross-sectional area ($\theta = 0$) and three with a curved cross-sectional area ($\theta > 0$). All the BPP geometries are listed in Table 2.

		d	w_c	w_l	r_{in}	r_{out}	θ
Anode	BPP-1	0.22	0.33	0.67	0	0	90
	BPP-2	0.24	0.35	0.84	0	0	90
	BPP-3	0.36	0.96	0.93	0	0	90
	BPP-4	0.22	0.219	0.562	0.1	0.155	116
	BPP-5	0.24	0.292	0.769	0.06	0.135	105
	BPP-6	0.36	0.752	0.733	0.15	0.25	120
Cathode	BPP-1	0.3	0.46	0.54	0	0	90
	BPP-2	0.3	0.58	0.61	0	0	90
	BPP-3	0.36	0.96	0.93	0	0	90
	BPP-4	0.3	0.347	0.435	0.1	0.175	110
	BPP-5	0.3	0.438	0.472	0.06	0.135	115
	BPP-6	0.36	0.752	0.733	0.15	0.25	120

Table 2: All tested BPP geometries

By using the Zwick, the force applied to the fixture is known, and the compressed pressure between the anode and cathode landings can be calculated by Eq. 4.

$$p_l = \frac{F}{L(w_p - N_{ch} w_{ch})} \tag{4}$$

where:

p_l = pressure at landing [Pa]

F = applied force [N]

L = channel length [m]

w_p = width of the plate [mm]

N_{ch} = number of parallel channels

and the w_{ch} is the total width of the channel, which can be calculated according to Eq. 5.

$$w_{ch} = w_c + d \cdot tan(\alpha - \frac{\pi}{2}) + r_{out}(sin\beta - \frac{(1 - cos\beta)}{tan\beta}) \tag{5}$$

where $\alpha = \pi \cdot \theta/180$ and $\beta = \pi - \alpha$.

3.3.2 Procedure

Initially, a force corresponding to a pressure of 2.0 MPa at the land, is applied to the fixture. A screw in the intrusion press is then tightened so the pressure is maintained during the time the fixture is moved over to the microscope (Leica DVM6 with objective PLANAPO FOV 15.55) where the thickness of the samples can be measured, and the intrusion can be observed.

Figure 12 shows how the measurement with the microscope is performed. The green line is for the sample thickness in a compressed state. The red lines are to measure the intrusion at the anode side, and the blue lines are for the cathode side. The intrusion is measured at 18 different points, two on each side outside the channel, and 14 points inside the channel.

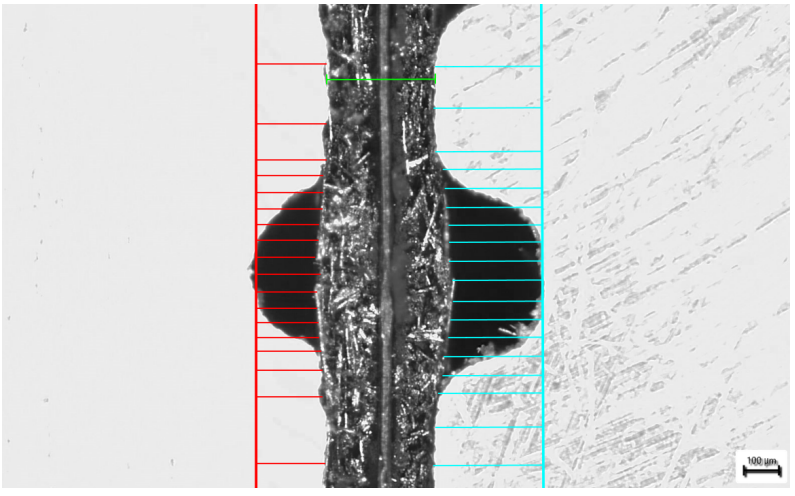

Figure 12: Image of how the measurement points is selected using the microscope.

The measurement is repeated for each channel on the BPP-template, and the test is repeated 3 times for each material and pair of BPP geometry.

3.4 Analytic Approximation Tool

3.4.1 Intrusion Line

Based on the results obtained from the intrusion measurements, it can be assumed that the maximum intrusion occurs at the center of the channel. The intrusion have a slightly bend profile with fixed endpoints at the metal walls of the BPP, which looks like a cosine curve, and therefore the function for the intrusion line is approximated according to Eq. 6.

$$f(x) = Ccos(\varphi x) \quad , x_1 \leq x \leq x_2 \tag{6}$$

where C describes the maximum deflection of the GDL out in the channel, i.e., the maximum intrusion. This parameter is assumed to depend on the pressure applied at the landing, the thickness of the sample, the bending properties of the material, as well as the BPP parameters that form the channel geometry. Equation 7 shows how C is defined.

$$C = \frac{w_c}{w_l}(t_{uncomp} - t_{comp}) \tag{7}$$

where:

t_{uncomp} = uncompressed thickness of the GDL material [µm]

t_{comp} = compressed thickness of the GDL material [µm]

The parameter φ describes the length of the channel and only depend on the BPP geometry, therefore it can be expressed according to Eq. 8.

$$\varphi = \frac{2\pi}{w_{ch}} \tag{8}$$

The valid interval is $x_1 \leq x \leq x_2$ for the function $f(x)$ and it marks where the intrusion line starts and ends in the channel, i.e., the range from where the GDL no longer holds contact with the BPP.

3.4.2 Stack Pressure Drop

During operation, both the anode and cathode channels can be seen as small pipes, and therefore, the stack pressure drop can be calculated according to Eq. 9.

$$\Delta p = f\frac{L}{D_H}\rho\frac{v^2}{2} \tag{9}$$

where:

f = friction factor

L = channel length [m]

ρ = fluid density [kg m $^{-3}$]

v = average velocity [m s^{-1}]

Here D_H is the hydraulic diameter [m] and is defined as $D_H = 4A_{ch}/P_{ch}$, and P_{ch} is the wetted perimeter. Since the flow is laminar, the friction factor can be approximated according to Eq. 10. The Reynolds number is defined as $Re = \rho v D_H/\mu$, where μ is the fluid dynamic viscosity.

$$f = \frac{64}{Re} \tag{10}$$

If the effect from the intrusion is considered, the cross-sectional area for the channel is changed. This will in turn affect the flow velocity (Eq. 11) and the hydraulic diameter needed to determine the pressure drop.

$$v = \frac{Q_{stack}}{N_{cell} N_{ch} A_{ch}} \tag{11}$$

where:

Q_{stack} = fluid rate at the stack entrance [m^3 s^{-1}]

N_{cell} = number of cells in the stack

N_{ch} = number of parallel channels in each cell

A_{ch} = cross-sectional area of the channel [m^2]

The fluid flow rate Q_{stack} can be calculated according to Eq. 12.

$$Q_{stack} = \frac{T_{in}}{T_0} \frac{p_0}{p_{in}} \frac{I \cdot S \cdot q \cdot N_{cell}}{c \cdot 60} \tag{12}$$

where:

T_0 = standard conditions for temperature = 273.15 [K]

p_0 = standard conditions for pressure = 1 [bar]

T_{in} = stack inlet temperature [K]

p_{in} = stack inlet pressure [bar]

I = stack current [A]

S = stoichiometry

q = volumetric flow rate (7.0 for hydrogen and 16.6 for air) [standard ml/cell/A/min]

c = gas concentration (1 = pure hydrogen /air)

The cross-sectional area, considering the intrusion effect can be expressed in terms of the difference from the area of the BPP channel, and the integral of the intrusion line function, which is described in Eq. 13.

$$A_{ch} = A_{BPP} - A_I = d \cdot w_c + d^2 \cdot tan(\alpha - \frac{\pi}{2}) + 2 \cdot (r_{out}^2 - r_{in}^2) \cdot (sin\beta - \\ - \frac{cos\beta \cdot sin\beta}{2} - \frac{\beta}{2} - \frac{(1 - cos\beta)}{2}^2 \cdot tan(\alpha - \frac{\pi}{2})) - \int_{x_1}^{x_2} f(x)dx \quad (13)$$

In Eq. 14 the contribution of the intrusion line has been added in the calculation of the wetted perimeter.

$$P_{ch} = P_{BPP} + P_{GDL} = w_c - 2 \cdot r_{in} \cdot (1 - cos\beta) \cdot (\frac{1}{tan\frac{\beta}{2}} - \frac{1}{tan\beta}) + 2 \cdot \beta \cdot (r_{out} + r_{in}) + \\ + 2 \cdot (\frac{d}{sin\beta} - (r_{out} + r_{in}) \cdot \frac{(1 - cos\beta)}{sin\beta}) + \int_{x_1}^{x_2} \sqrt{1 + f'(x)^2} dx \quad (14)$$

4 Results & Discussion

4.1 GDL Characteristics

4.1.1 Compression Test

The initial thickness of the samples was measured during the compression test. At the very low pressure of 0.025 MPa, sample C is the thinnest of the measured materials with a thickness of 166.3 µm. Sample A has a thickness of 191.9 µm, while the sample B thickness is 186.2 µm. Among the measured MEA's, sample C is measured to 387.7 µm, compared to samples A and B with thicknesses 422.5 and 394.9 µm, respectively. At 2.0 MPa sample C is still the thinnest material for both a single layer GDL and MEA. A summary of the compressed thicknesses, for samples A, B and C, after the first cycle for both 0.025 and 2.0 MPa is available in Table 3, where the deviation is also presented.

	A	B	C
Single GDL @ 0.025 MPa [µm]	191.9 ± 4.3	186.2 ± 8.1	166.3 ± 3.6
Single GDL @ 2.0 MPa [µm]	132.3 ± 2.0	136.6 ± 4.5	125.6 ± 0.9
MEA @ 0.025 MPa [µm]	422.5 ± 10.6	394.9 ± 6.8	387.7 ± 6.0
MEA @ 2.0 MPa [µm]	321.8 ± 4.2	318.8 ± 2.9	299.6 ± 1.0

Table 3: The thickness at first cycle.

In Fig. 13 it can be seen that the GDL is deformed after the 1st cycle. For the single-layer GDL, the thickness at the 2nd cycle at 0.025 MPa is 159.5 µm for material A, 153.1 µm for B, and 150.0 µm for C. At the 3rd cycle, the thickness has been reduced less than 1 µm for all materials, and in the 4th cycle, the thickness is further reduced by a few tens of µm. The thickness at the 2nd cycle for the MEA is 378.6 µm for A, 357.0 µm for B, and 358.7 µm for C. For the 3rd and 4th cycle the thickness continues to shrink. Between the two last cycles, the materials have reduced their thicknesses with 1.6 µm for A, 1.1 µm for B, and 0.8 µm for C.

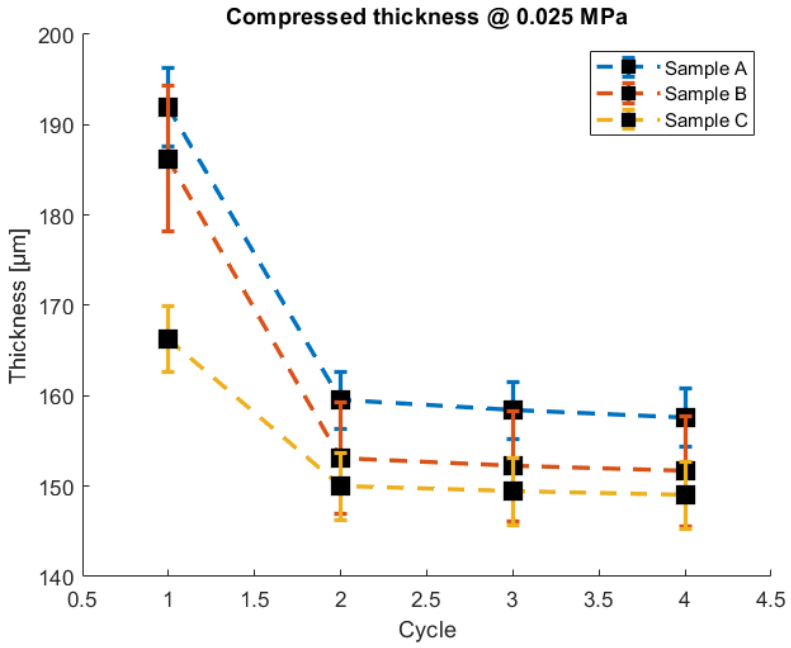

(a)

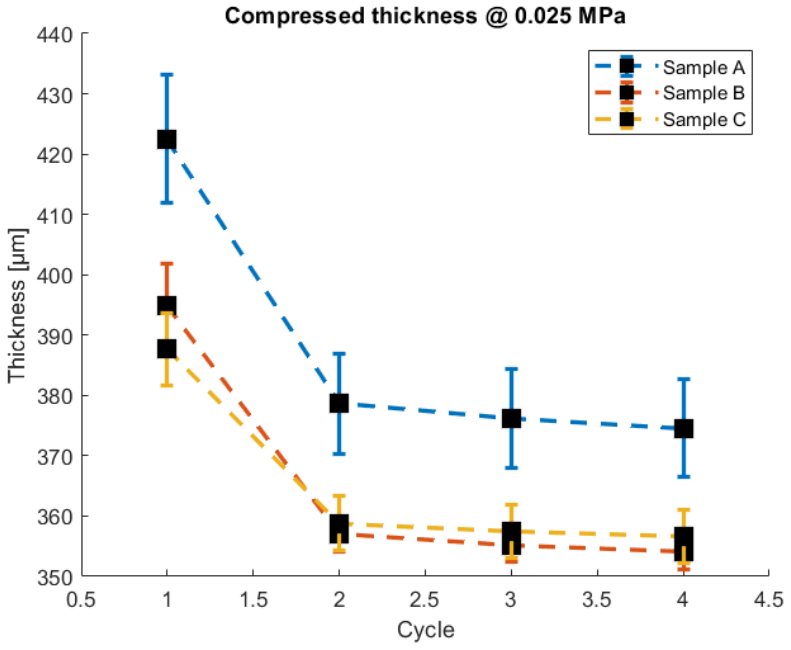

(b)

Figure 13: The thickness at 0.025 MPa for each cycle.

The results for the compressed thicknesses at 2.0 MPa are available in Fig. 14, and

as for the lower pressure, the biggest difference occurs between the 1st and 2nd cycle, and the smallest difference is between the 3rd and 4th cycle. The magnitude for the biggest gap is for a single GDL ∼1 µm, and less than a half µm for the smallest gap. In the case regarding the MEA's, the largest gap differs between 1-2.5 µm, while the smallest is about 1 µm for material A and 0.4 µm for both B and C.

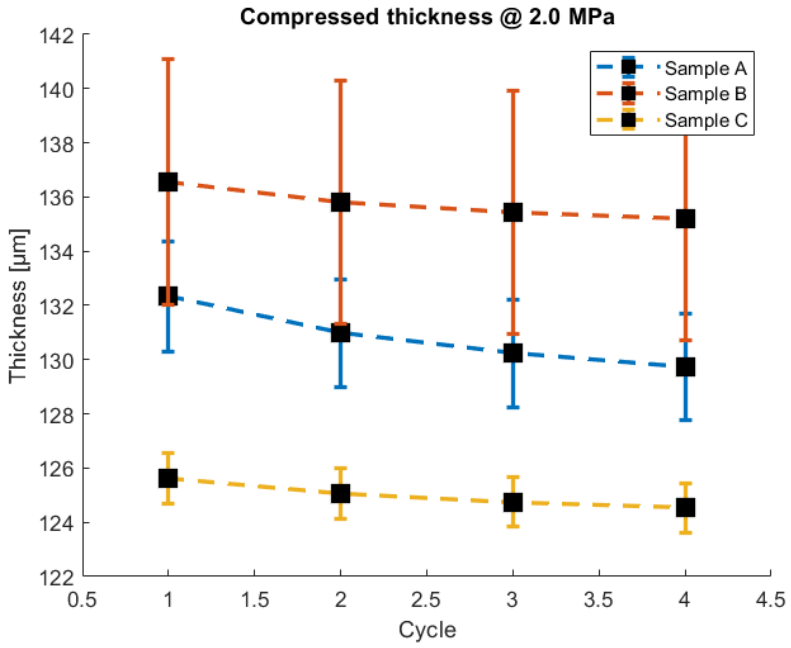

(a)

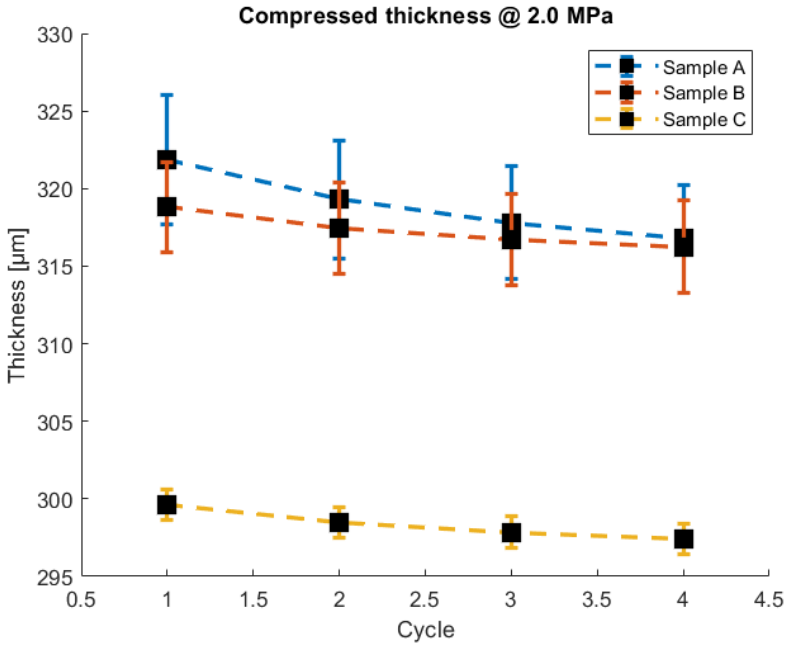

(b)

Figure 14: The thickness at 2 MPa for each cycle.

4.2 Intrusion Measurements

The results from the measured intrusion profiles can be seen in Figs. 15-20, where the profiles are plotted in relation to the BPP geometry. The red series is for sample A, the green for sample B, and the blue for sample C. In every graph, material A stands out with its slightly higher intrusion shape, while materials B and C are more similar. It can also be seen that the maximal intrusion is found in the center of the channel and that the plotted profiles have a small bent look.

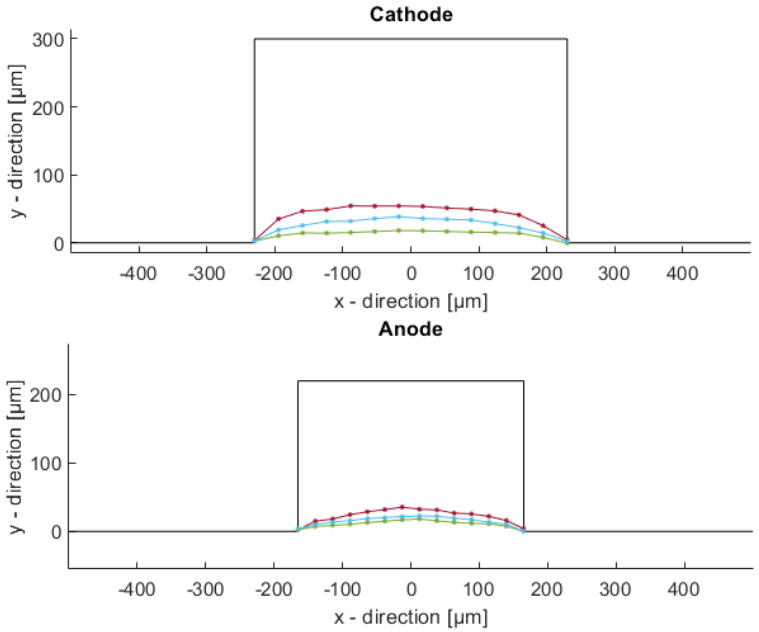

Figure 15: BPP-1

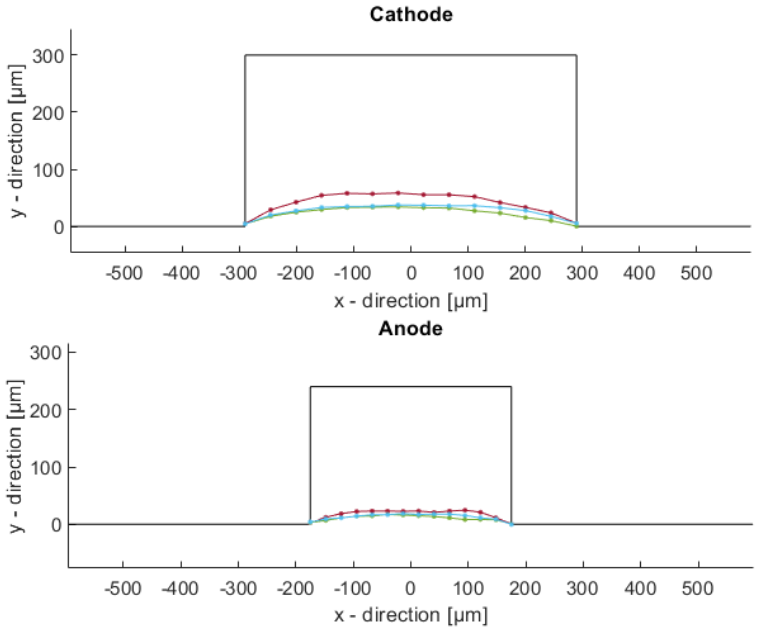

Figure 16: BPP-2

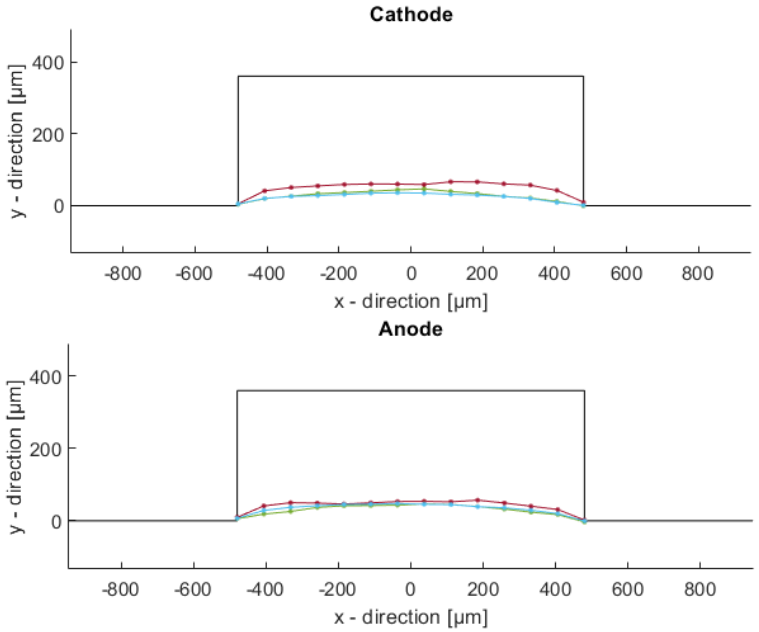

Figure 17: BPP-3

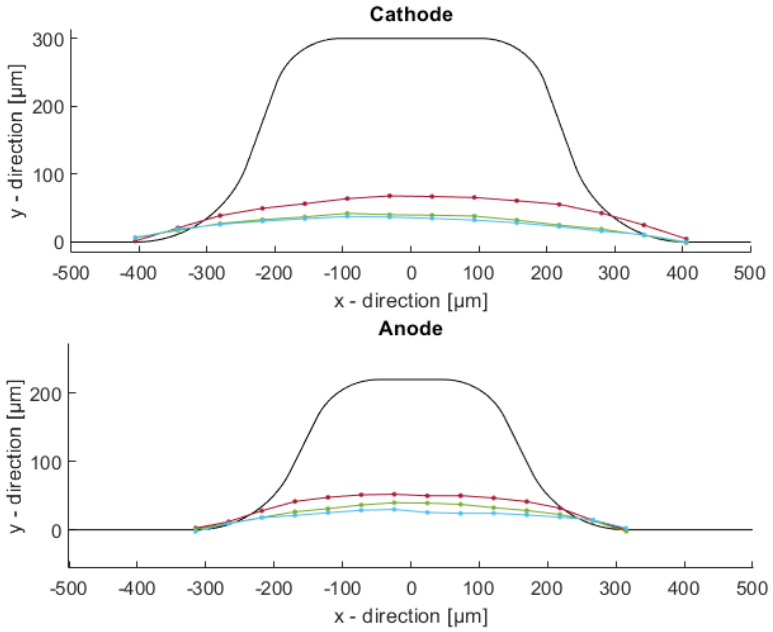

Figure 18: BPP-4

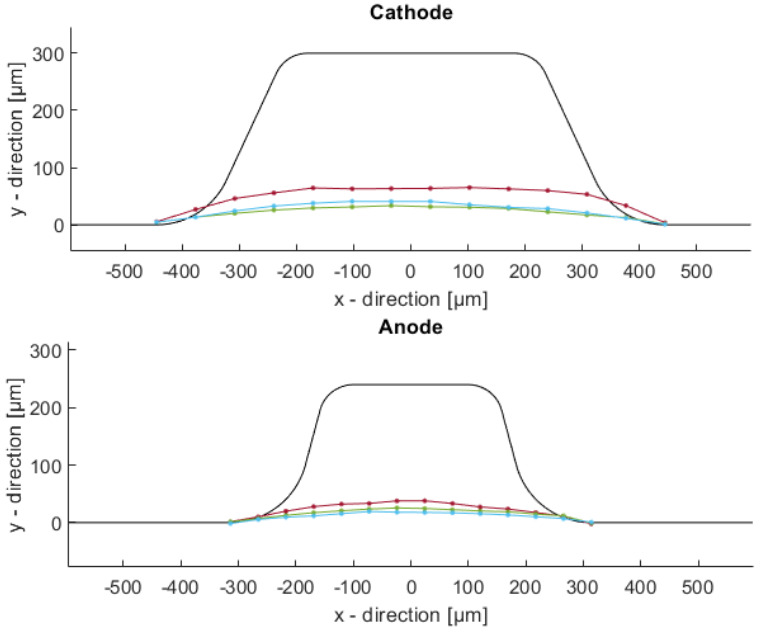

Figure 19: BPP-5

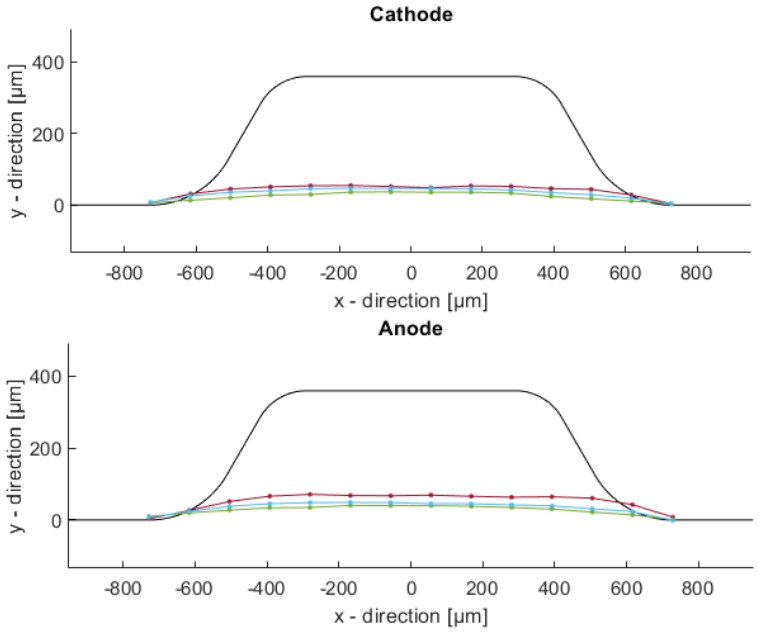

Figure 20: BPP-6

In Figs. 21-23 the maximum intrusion is presented together with the deviation. Overall, it can be seen that the cathode channel generates higher intrusion than the anode channel. By first study the rectangular-shaped cross-sectional area, the widest channel (BPP-3) is found to be where the intrusion is highest. For the curved BPP templates, it can only be seen for material C that the maximum intrusion occurs in the widest channel. Even so, it can clearly be seen that the smallest channels (BPP-1 and BPP-2 anode) have a much lower maximum value in contrast to the widest (BPP-3 and BPP-6), and a conclusion can therefore be drawn that intrusion depends on the channel width.

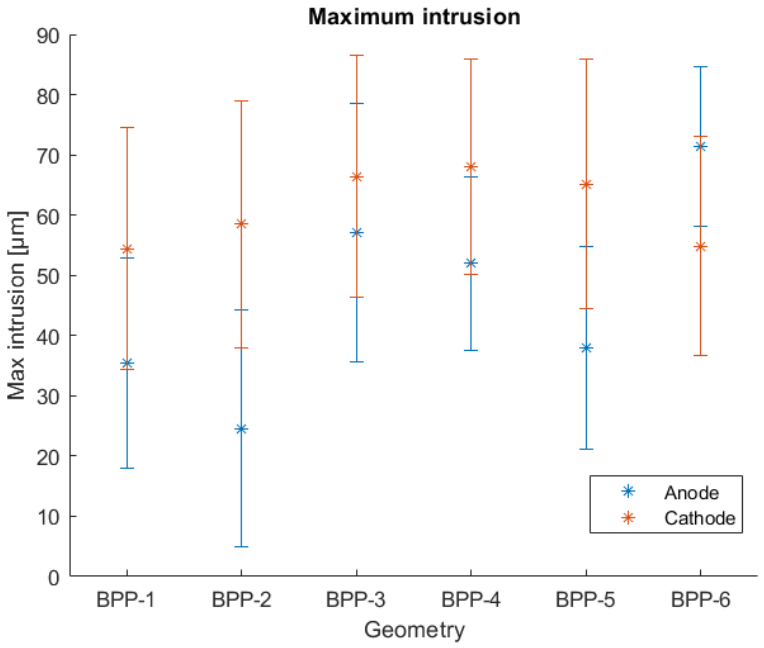

Figure 21: The maximal intrusion for material A.

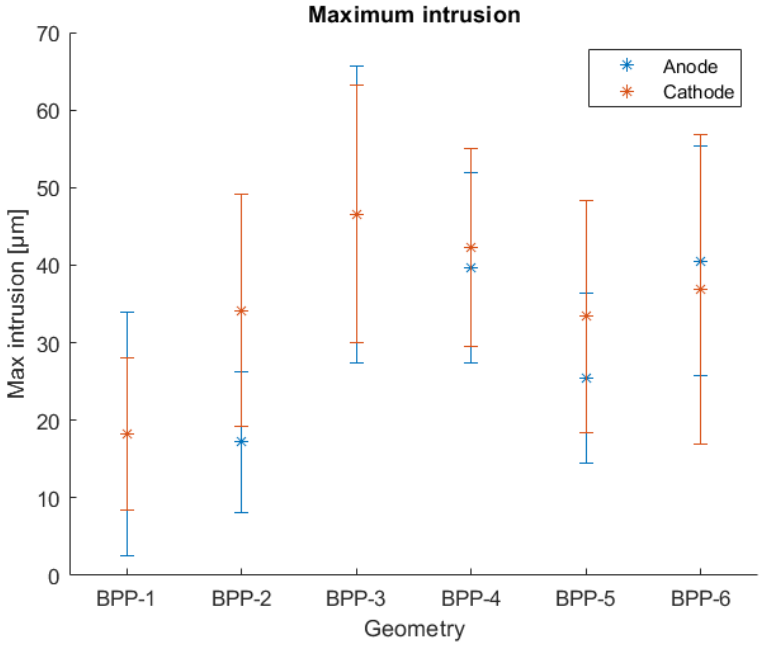

Figure 22: The maximal intrusion for material B.

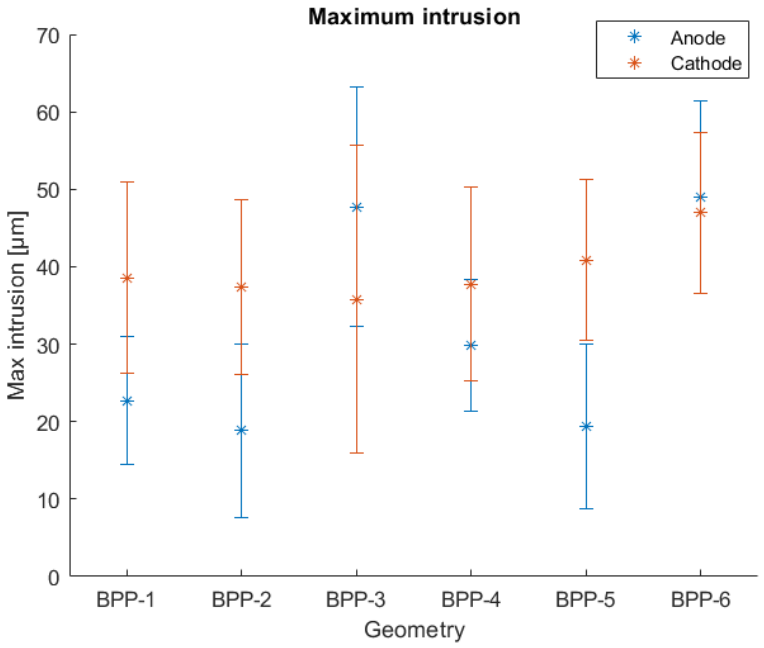

Figure 23: The maximal intrusion for material C.

A potential error source in these measurements could be the application of the force, which could result in invalid data. First, the force is calculated, but the calculations are based on the exact dimensions for the BPP templates. The precise dimensions and tolerances are difficult to obtain during manufacturing, and therefore a small error can be found here. In Fig. 24 the manufactured channels are visualized.

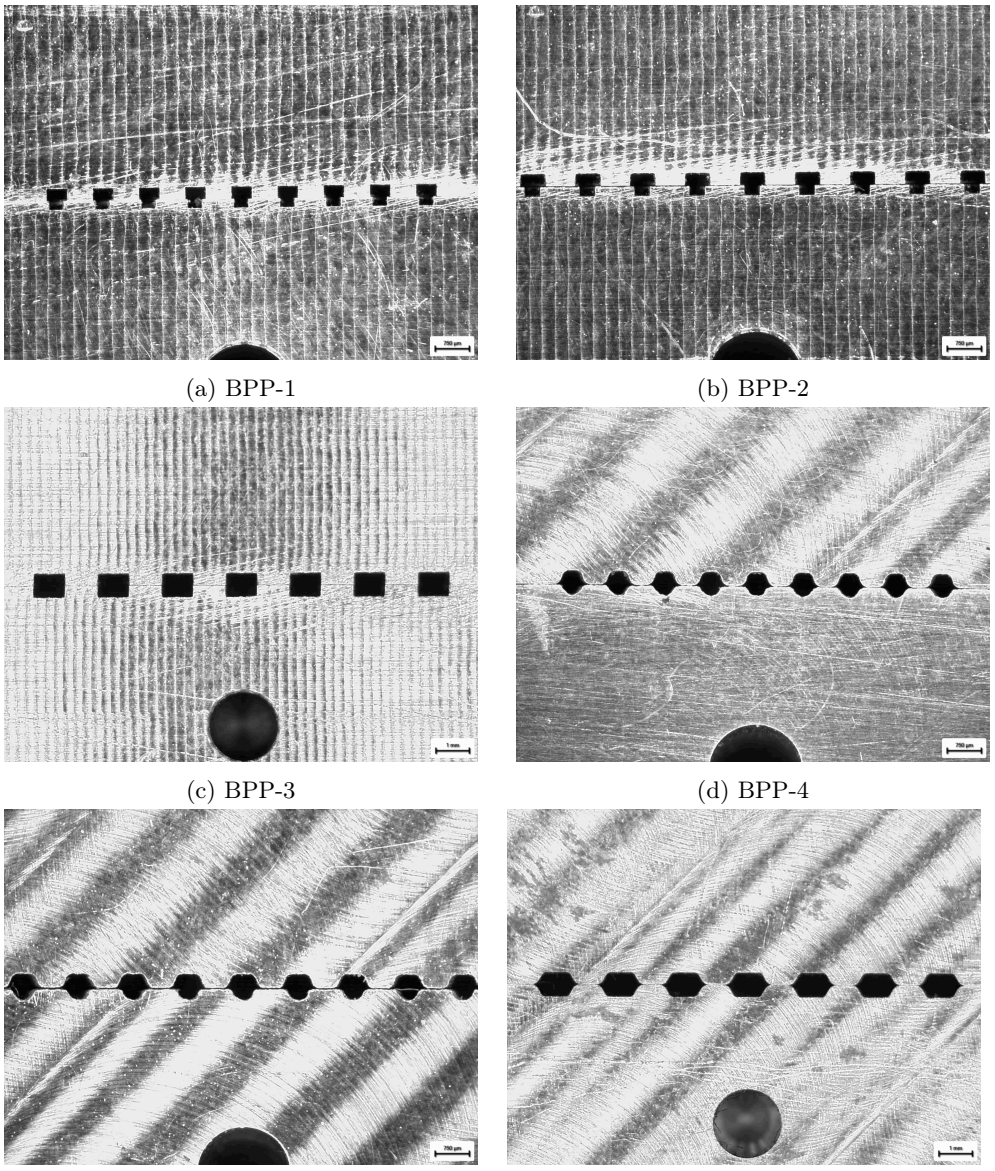

(a) BPP-1 (b) BPP-2

(c) BPP-3 (d) BPP-4

(e) BPP-5 (f) BPP-6

Figure 24: Images of the channels on the BPP templates.

Second, the force is applied in the Zwick where the screw is tightened manually. Due to the manual maneuver, a small force is added to the fixture which unbalances the force regulation in the machine. According to the information from the Zwick software, the force applied to the fixture can differ within ± 10 N.

To make sure the force was applied correctly the compressed thickness was measured and compared with the data obtained in the compression test. The compressed thicknesses from the intrusion measurements are summarized in Fig. 25. By studying

material C it can be seen that the compressed thickness is close to the values obtained from the compression test (± 15 µm off), which indicates that the force is applied almost correctly. For material B the values are about a few micrometers offset if the value for BPP-4 is neglected. The same is valid for material A, but where the values are offset by over 25 µm.

The force can be assumed to be applied correctly with a small error, due to the manufacturing defects from the BPP template and the human factor when tightening the screw. However, as seen from the compression test there might be a bigger deviation for all the GDL thicknesses. This could explain the offset seen in Fig. 25.

Another explanation for the offset is the impact of shear stresses in the GDL under the land. A hypothesis would be that material C has the highest shear modulus and that A has the lowest. This could mean that part of material A is pressed out to the channel, resulting in less material under the compressed land surface. The shear modulus for B would be somewhere between the value for A and C, which is why less material is pressed from the land compared to material A, explaining why the offset is not equal for these two materials. The modulus for material C could be high enough to not result in any change, which would make sense since there is non offset observed for this material. However, if this is the reason for the offset from the measured compressed values in Fig. 25, it should be verified and further investigated on what kind of effect this gives on intrusion.

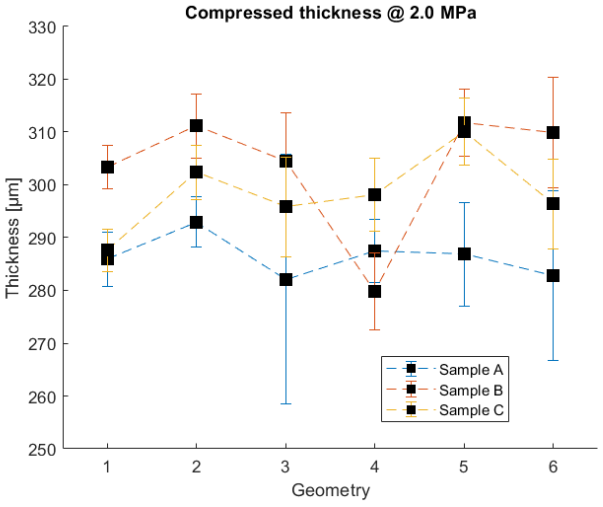

Figure 25: The compressed thicknesses from the intrusion measurements.

Another error source is the number of tested samples. It is difficult to see in Figs. 21-23 if there is a correlation between intrusion and the channel geometry. This indicates that too few series have been tested to have a stochastic result to analyze. The same indication is found in Fig. 25 where the deviation for BPP-3 and BPP-6 is significantly higher relative to the rest of the geometries. All BPP templates have 9 channels and have been tested two times, except BPP-3 and BPP-6 which have 7 channels, and have instead been tested three times. This means that there

are more collected data for these two geometries, and therefore it seems reasonable that the deviation is higher. A minor error could also occur during the selection of measurement points in the microscope, which would also benefit from collecting more data so that the total error could be negligible.

While studying the intrusion profile in the microscope, several GDL defects have been detected. Examples of how these defects look like can be seen in Fig. 26. Some of the defects are believed to emerge from the cutting process and while mounting the samples into the intrusion test fixture. Other defects can arise from the compression stage where the GDL is deformed and fibers break.

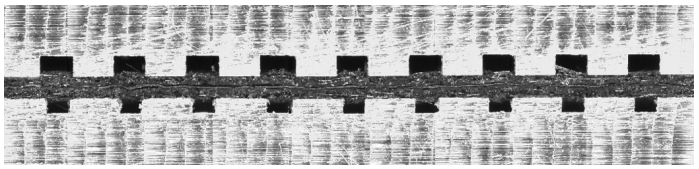

(a) Material A in BPP-1

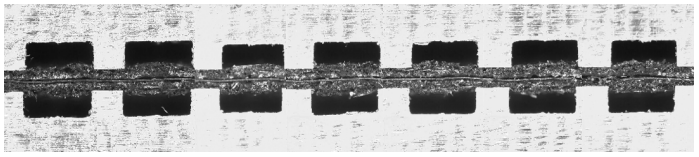

(b) Material A in BPP-3

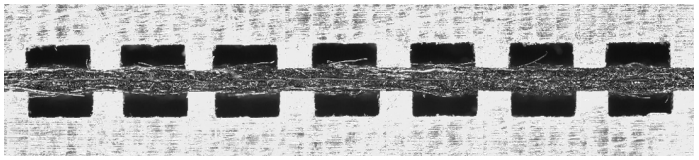

(c) Material B in BPP-3

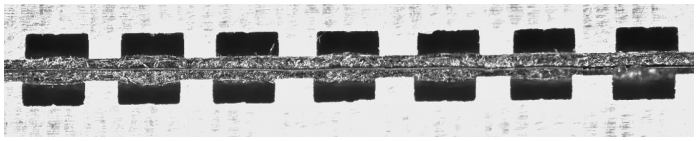

(d) Material C in BPP-3

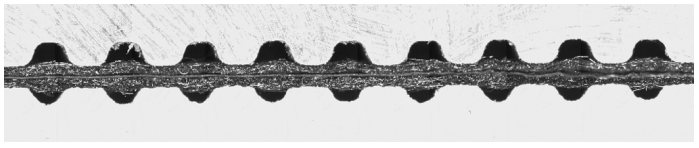

(e) Material B in BPP-4

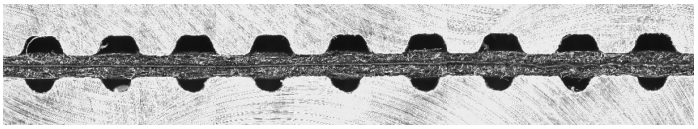

(f) Material C in BPP-5

Figure 26: Images of the intrusion profile and GDL defects observed in the microscope.

As can be seen in the images, and in Table 4, fibers are more likely to break in the channels with $\theta = 0$, compared to the ones where $\theta > 0$. The reason for this behavior is believed to be related to how the force is distributed under the land where the compression takes place. With a curved edge, the force is more smoothly distributed which is less harmful to the fiber.

	A	B	C
BPP-1	39%	11%	22%
BPP-2	28%	44%	28%
BPP-3	14%	43%	10%
BPP-4	17%	11%	6%
BPP-5	6%	11%	11%
BPP-6	5%	5%	5%

Table 4: Detected GDL defects in the channels.

How accurate is this method to study the intrusion phenomenon? The boundary conditions for the fibers are not quite the same as for an assembled fuel cell. In the fuel cell, the bulk properties of the GDL will support the surrounded fibers, and therefore gain a higher mechanical strength compared to the case in this work where the fibers have been cut and the edge of the sample is studied. Hence, this method is assumed to over-predict the actual intrusion that occurs in a fuel cell. To verify this assumption, the intrusion phenomenon should be studied with a new approach. An alternative method could be to infuse the BPP and MEA in epoxy and grind to a suitable cross-section that would be fitted to study. This could also be an alternative to minimize defects that occurs during the cutting process.

4.3 Approximation Tool

4.3.1 The Intrusion Line

From the assumptions stated based on the results from the intrusion measurements, the intrusion profile is approximated as the function, $f(x)$. In Figs. 27, 28, and 29 both the results from the intrusion measurements (dashed lines) and the approximated function (solid lines) are presented.

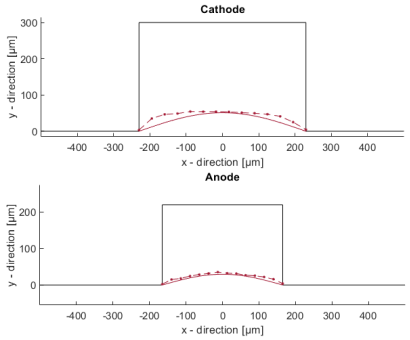

(a) BPP-1

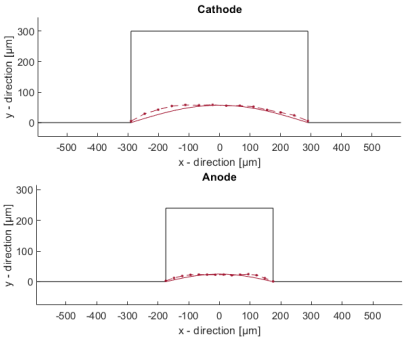

(b) BPP-2

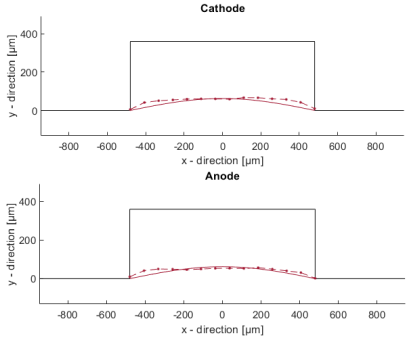

(c) BPP-3

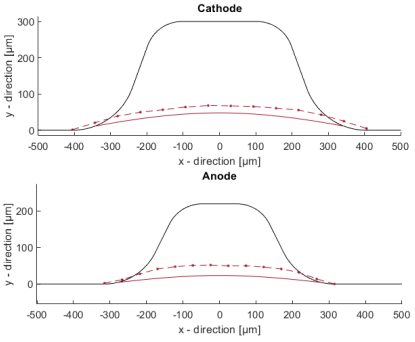

(d) BPP-4

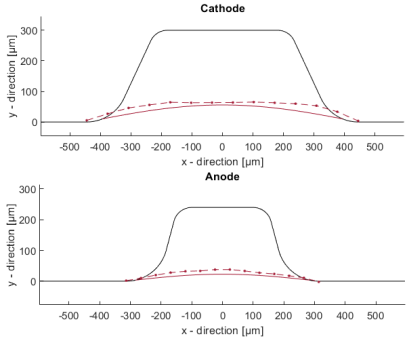

(e) BPP-5

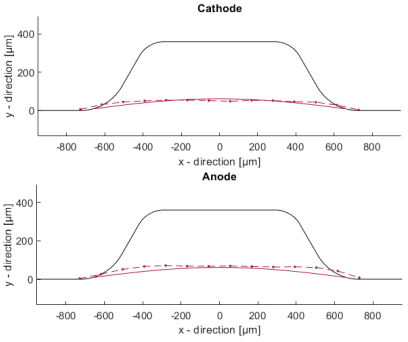

(f) BPP-6

Figure 27: A comparison between the measured and approximated results for material A.

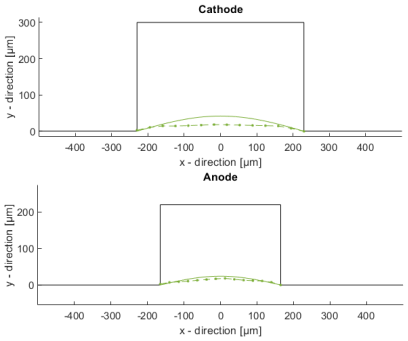

(a) BPP-1

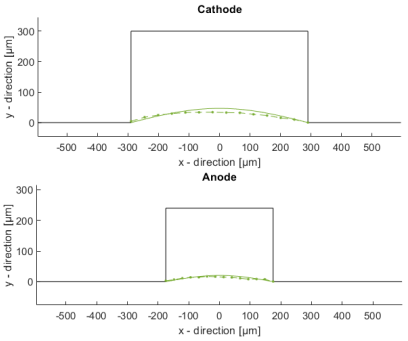

(b) BPP-2

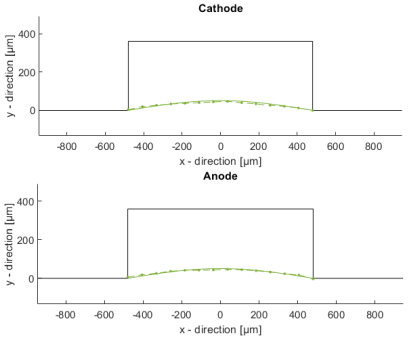

(c) BPP-3

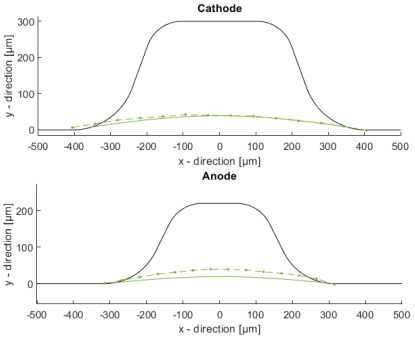

(d) BPP-4

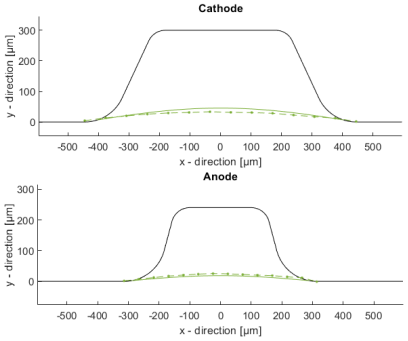

(e) BPP-5

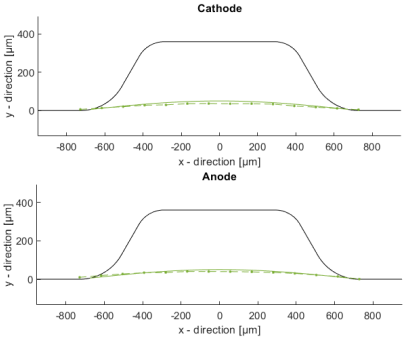

(f) BPP-6

Figure 28: A comparison between the measured and approximated results for material B.

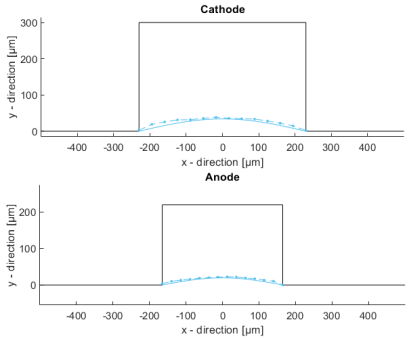

(a) BPP-1

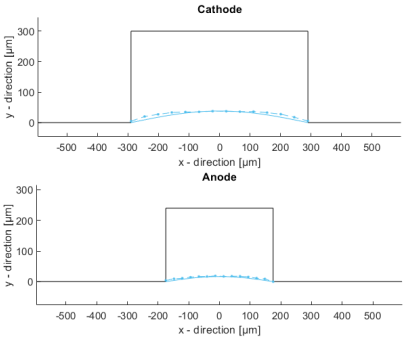

(b) BPP-2

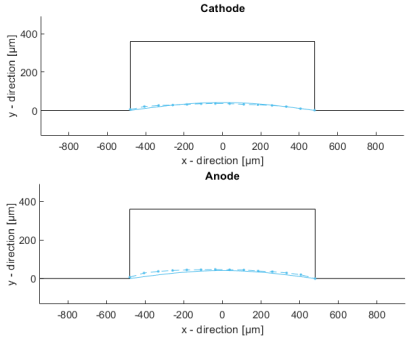

(c) BPP-3

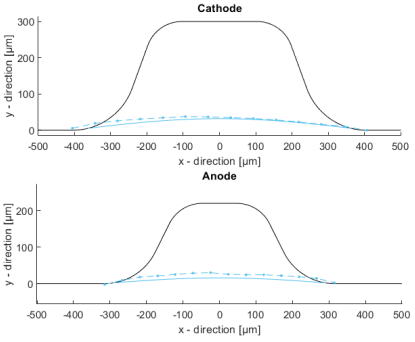

(d) BPP-4

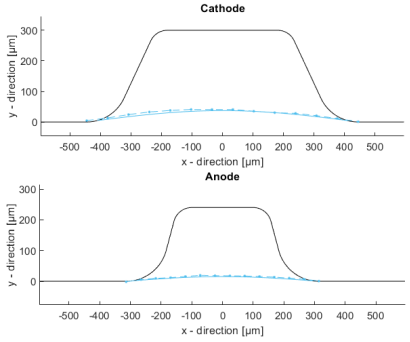

(e) BPP-5

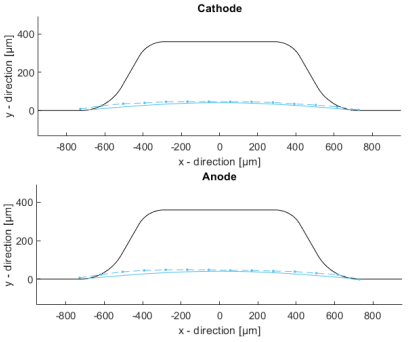

(f) BPP-6

Figure 29: A comparison between the measured and approximated results for material C.

It can clearly be seen that for most of the cases both the measured and approximated results intersect almost perfectly with each other. There are three cases that stand out and have a higher error margin compared to the rest; BPP-4 for material A, BPP-1 cathode for material B, and BPP-4 anode for material B. By studying Fig. 21 it can be seen that the maximum intrusion for both channels on the BPP-4 geometry is quite high compared to the geometries of the same size, which seems most unlikely. These samples can be stated to include several errors or defects.

Regarding the two divergent channels for material B, the same argument as above can be applied. From Fig. 22 it can be seen for BPP-1 that the anode and cathode values are more or less equal. The maximum intrusion value for the cathode might be a bit low compared to other values, which for the other materials shows it should be close to the cathode value for BPP-2. By instead studying the values for BPP-4, these values seem also to be a bit off. By disregarding these 3 noted cases, it can otherwise be stated that the approximated function fits well with the measured results with only a small error.

Another observation is that the cosine curve may not be a successful fit for material A. The approximated function aligns well in the center of the channel, but the error rises closer to the channel walls. This indicates that this choice of approximated function will not work for larger intruded materials.

4.3.2 The Stack Pressure Drop

Based on the predicted intrusion profiles, the stack pressure drop can be calculated. A case including the BPP-5 geometry and the GDL materials (A, B, and C) is studied. The input parameters, such as $I = 1000$ A, $L = 260$ mm, $N_{cell} = 20$ and $N_{ch} = 102$, along with the values specific for the anode and cathode side are presented in Table 5. The intrusion profiles for this stack is presented in Fig. 30, and Fig. 31 shows the result for the stack pressure drop.

	Anode	Cathode
S	1.5	1.8
c	0.7	1
T_{in} [°C]	70	70
p_{in} [bar]	3.0	3.0
ρ [kg/m^3]	1.04	2.99
μ [N s/m^2]	$1.586 \cdot 10^{-5}$	$2.3 \cdot 10^{-5}$

Table 5: Input parameters used for the pressure drop calculation

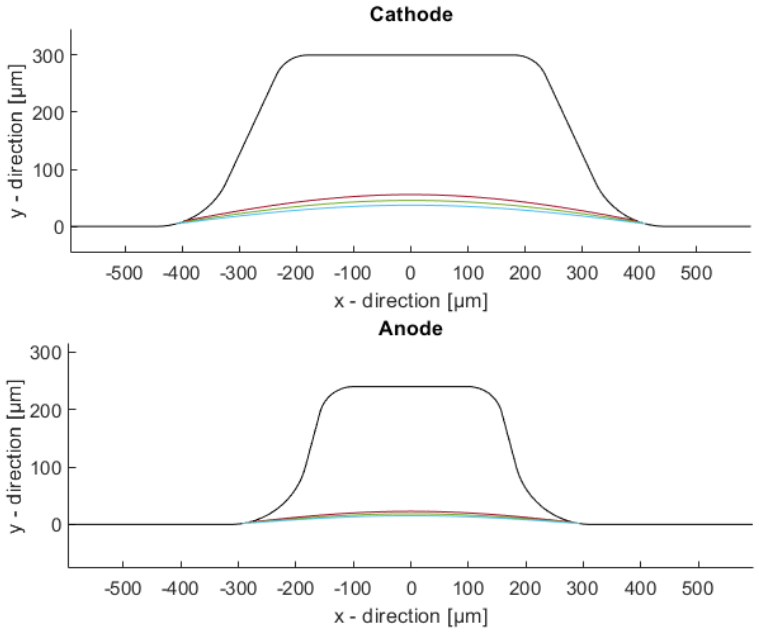

Figure 30: The approximated intrusion profiles.

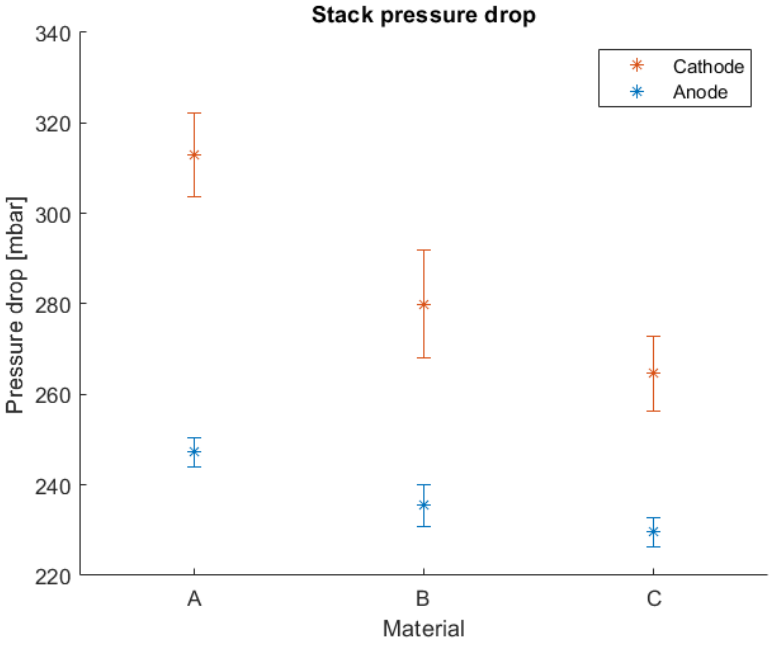

Figure 31: The output from the pressure drop calculations.

Both materials A and B have been used in a fuel cell stack test with similar input parameters used in this case. Comparing the measured stack pressure drop values from the tests with the calculated results here, it is found that the values are in the same order of magnitude and relation to each other, only that the calculated values are lower (see Table 6) except for material B on the cathode side.

		Approximated values [mbar]	Measured values [mbar]
Anode	Material A	247	251
	Material B	235	212
Cathode	Material A	313	376
	Material B	280	309

Table 6: Summary of the stack pressure drop results.

It is expected to find that the approximated values don't correspond to the reality, since the case only considers the pressure drop over the total number of channels. The measured values are measured over the whole stack including the fluid flow inlet, main channel, BPP transition area, and the channels.

From CFD simulations, this case gives rise to a pressure drop of approximately 30 mbar over the BPP transition area. It also shows that the stack inlet and main channels appear as minor losses, and can be neglected.

A big difference in regarding the approximated values compared to the measured is the fluid flow which in reality is humidified. In this work, dry gases have been assumed to enter the fluid inlet because of simplicity. If the fluid flow would be considered humidified, the total fluid flow would increase, hence also increasing the pressure drop. From the CFD simulations there is almost 10 mbar difference on the pressure drop between dry and wet gases.

Overall, it can clearly been seen that the major losses for the stack pressure drop rise from the channels and intrusion effect.

5 Conclusions

The compressive behavior of GDL was investigated for three materials at a load from 0.025 MPa to 2.0 MPa and found to be irreversible. Material A was measured to be the thickest of the materials for both a single layer GDL and assembled as a MEA, followed by materials B and C. Under cyclic compression all materials show a settling behavior, minimizing the gap between the thickness for each cycle. Between the 3rd and 4th cycles, the thickness has decreased less than half a µm for all single layer GDL, and for the MEA the thickness has reduced to 1 µm for material A and less than 0.4 µm for B and C.

With help from the data obtained from the compression tests, the intrusion was measured for 6 different geometries. The intrusion profile was found to depend on the channel width, where the largest intrusion occurs in the widest channel and the lowest intrusion in the smallest geometry. For all geometries, the intruded profile has a small bend shape, together with the maximum intrusion taking place in the center of the channel.

Based on all results from the measurements, an approximation was made to calculate the intrusion function that simulates the intruded profile that occurs for a given BPP geometry. The function was approximated as a cosine function with an amplitude depending on the channel-to-rib ratio of the BPP multiplied with the difference of uncompressed and compressed thickness of the GDL. The function was found to fit well with the measured values for materials B and C but seemed not to be as successful for material A.

Based on the results from the stack pressure drop calculations, it can be concluded that material A will demand most of the system output, followed by material B. It can therefore be stated that the most efficient material to use in respect to the intrusion and pressure drop is C. However, if this actually is the most efficient material to use is yet unknown since parameters like gas permeability, electrical and thermal conductivity have not been considered, and will influence the actual stack energy output.

6 Recommendations & Future Work

In this work, ambient conditions have been set to room temperature when performing all measurements. It might be of interest to see if any parameters change at a temperature closer to the one used in an operating fuel cell. Does the temperature influence the behaviour of the GDL during compression? If so, how does that affect the intrusion phenomenon?

How does this method work for other GDLs where the material could possibly intrude more into the channel? There is maybe a better function $f(x)$ that could be used to approximate the intrusion line. Such a function could also consider the misalignment of anode and cathode channels, or this case would perhaps need a separate function and assumptions. As stated in the theory chapter, there are several parameters influencing the intrusion. How can all of them be taken into consideration?

Regarding the calculations for the pressure drop, it could be further developed by taking humidified fluid flow into consideration, making the approximation more accurate. Further, to actually enable calculation of the whole tack pressure drop, a method to predict the influence of the BPP transition area should also be added. When proceeding to study the fluid flow and its influence, some attention should also be paid to the broken fibers and GDL defects that can disturb the homogeneous channel pattern. Is there a risk with having broken fibers and if, what would that imply?

References

[1] B. Sundén *"Hydrogen, Batteries and Fuel Cells"* (2019) Academic Press

[2] F. Barbir *"PEM Fuel Cells - Theory and Practice"* (2013) Academic Press

[3] [Illustration] *https://powercell.se/en/how-do-fuel-cells-work* (Retrieved 2022-01-05)

[4] A.L. Dicks *"The role of carbon in fuel cells"* Journal of Power Sources 156 (2006) 128-141

[5] X. Zhao, Y. Fu, W. Li, A. Manthiram *"Effect of non-active area on the performance of subgasketed MEAs in PEMFC"* International Journal o Hydrogen Energy (2013) 7400 - 7406

[6] B D. Agarwal, L J. Broutman, K. Chandrashekhara *"Analysis and performance of fiber composites third edition"* (2006) Wiley

[7] Y. Wang, C.W, K.S. C *"Elucidating differences between carbon paper and carbon cloth in polymer electrolyte fuel cells"* Electrochimica Acta 52 (2007) 3965 - 3975

[8] A. El-kharouf, B G.Pollet *"Chapter 4 - Gas Diffusion Media and their Degradation"* Polymer Electrolyte Fuel Cell Degradation (2012) 215-247

[9] M.Mortazavi, K. Tajiri *"Effect of the PTFE content in the gas diffusion layer on water transport in polymer electrolyte fuel cells (PEFCs)"* Journal of Power Sources 245 (2014) 236-244

[10] S.G. Kandlikar, Z. Lu, T.Y. Lin, D. Cooke, M. Daino *"Uneven gas diffusion layer intrusion in gas channel arrays of proton exchange membrane fuel cell and its effects on flow distribution"* Journal of Power Sources 194 (2009) 328 - 337

[11] F. Aldakheel, M.S Ismail, K.J Hughes, D.B Ingham, L. Ma, M. Pourkashanian, D. Cumming, R.Smith *"Gas permeability, wettability and morphology of gas diffusion layers before and after performing a realistic ex-situ compression test"* Renewable Energy 151 (2020) 1082 - 1091

[12] J. Kleemann, F. Finsterwalder, W.Tillmetz *"Characterisation of mechanical behaviour and coupled electrical properties of polymer electrolyte membrane fuel cell gas diffusion layers"* Journal of Power Sources 190 (2009) 92-102

[13] S. Mahabunphachai, Ö. Necati Cora, M. Koc *"Effect of manufacturing processes on formability and surface topography of proton exchange membrane fuel cell metallic bipolar plates"* Journal of Power Sources 195 (2010) 5269-5277

[14] A. Kim, H. Jung, S. Um *"An engineering approach to optimal metallic bipolar plate design reflecting gas diffusion layer compression effects"* Energy 66 (2014) 50 - 55

[15] L. Peng, P. Yi, X. Lai *"Design and manufacturing of stainless steel bipolar plates for proton exchange membrane fuel"* International Journal of Hydrogen Energy 39 (2014) 21127-21153

[16] P. Liang, D. Qiu, L. Peng, P. Yi, X. Lai, J. Ni *"Contact resistance prediction of proton exchange membrane fuel cell considering fabrication characteristics of metallic bipolar plates"* Energy Conversion and Management 169 (2018) 334-344

[17] S. Haase, M.Rauber *"Ex-situ diffusion layer intrusion effect determination of polymer electrolyte membrane fuel cell flow fields"* Journal of Power Sources 291 (2015) 246-254

[18] C. Tötzke, G. Gaiselmann, M. Osenberg, J. Bohner, T. Arlt, H. Markötter, A. Hilger, F. Wieder, A. Kupsch, B.R. Müller, M.P. Hentschel, J. Banhart, V. Schmidt, W. Lehnert, I. Manke *"Three-dimensional study of compressed gas diffusion layers using synchrotron X-ray imaging"* Journal of Power Sources 253 (2014) 123-131

[19] V. Radhakrishnan, P. Haridoss *"Effect of cyclic compression on structure and properties of Gas Diffusion Layer used in PEM fuel cells"* International Journal of Hydrogen Energy 35 (2010) 11107-11118

[20] K.D Baik, B.K. Hong, K. Han, M.S. Kim *"Correlation between anisotropic bending stiffness of GDL and land/channel width ratio of polymer electrolyte membrane fuel cell"* International Journal of Hydrogen Energy 37 (2012) 11921-11933

[21] E. Hoppe, H. Janßen, M. Müller, W. Lehnert *"The impact of flow field plate misalignment of the gas diffusion layer intrusion and performance of a high-temperature polymer electrolyte fuel cell"* Journal of Power Sources 501 (2021) 230036

[22] J. Hoeflinger, P. Hofmann *"Air mass flow ad pressure optimisation of a PEM fuel cell range extender system"* International Journal of Hydrogen Energy 45 (2020) 29246 - 29258

[23] J. Schröter, T. Graf, D. Frank, C. Bauer, J. Kallo, C. Willich *"Influence of pressure losses on compressor performance in a pressurized fuel cell air supply system for airplane applications"* International Journal of Hydrogen Energy 46 (2021) 21151 - 21159